Saturation of the compression of two interacting magnetic flux tubes evidenced in the laboratory

A. Sladkov,[1] C. Fegan,[2] W. Yao,[3,4] A.F.A. Bott,[5] S. N. Chen,[6] H. Ahmed,[7] E.D. Filippov,[8] R. Lelièvre,[3,9] P. Martin,[2] A. McIlvenny,[2] T. Waltenspiel,[3] P. Antici,[10] M. Borghesi,[2] S. Pikuz,[11] A. Ciardi,[4] E. d'Humières,[12] A. Soloviev,[13] M. Starodubtsev,[13] and J. Fuchs[3,*]

[1]*Light Stream Labs LLC, USA, Palo Alto, CA 94306*
[2]*Center for Plasma Physics, School of Mathematics and Physics, Queen's University Belfast, Belfast BT7 1NN, United Kingdom*
[3]*LULI - CNRS, CEA, UPMC Univ Paris 06 : Sorbonne Université, Ecole Polytechnique, Institut Polytechnique de Paris - F-91128 Palaiseau cedex, France*
[4]*Sorbonne Université, Observatoire de Paris, Université PSL, CNRS, LERMA, F-75005, Paris, France*
[5]*Department of Physics, University of Oxford, Parks Road, Oxford OX1 3PU, United Kingdom*
[6]*ELI-NP, "Horia Hulubei" National Institute of Physics and Nuclear Engineering, Bucharest - Magurele, Romania*
[7]*STFC, U.K.*
[8]*CLPU, 37185 Villamayor, Spain*
[9]*Laboratoire de micro-irradiation, de métrologie et de dosimétrie des neutrons, PSE-Santé/SDOS, IRSN, 13115 Saint-Paul-Lez-Durance, France*
[10]*INRS-EMT, 1650 boul, Lionel-Boulet, Varennes, QC, J3X 1S2, Canada*
[11]*HB11 Energy Holdings, Freshwater, NSW 2096, Australia*
[12]*University of Bordeaux, Centre Lasers Intenses et Applications, CNRS, CEA, UMR 5107, F-33405 Talence, France*
[13]*Independent Researcher*

Interactions between magnetic fields advected by matter play a fundamental role in the Universe at all possible scales. A crucial role these interactions play is in making turbulent fields highly anisotropic, leading to observed ordered fields. These in turn, are important evolutionary factors for all the systems within and around. Despite scant evidence, due to the difficulty in measuring even near-Earth events, the magnetic field compression factor in these interactions, measured at very varied scales, is limited to a few. However, compressing matter in which a magnetic field is embedded, results in compression up to several thousands. Here we show, using laboratory experiments and matching three-dimensional hybrid simulations, that there is indeed a very effective saturation of the compression when two independent magnetic fields are advected by plasmas encounter. We found that the observed saturation is linked to a build-up of the magnetic pressure at the inflows encounter point, which decelerates them and thereby stops further compression. Moreover, the growth of an electric field, induced by the incoming flows and the magnetic field, acts in redirecting the inflows transversely, further hampering field compression.

To investigate magnetic field compression in a setting that is frequently encountered in the Universe, i.e. that of two interacting independent large-scale magnetic structures, we use two high-power lasers (see Methods) to generate [1, 2] two independent magnetic flux tubes (with field strength $\sim$ 100 T [see Methods]), that counter-propagate toward each other at super-Alfvénic velocity. The top view of the experimental setup is shown in Fig. 1 (a). As shown by the time-resolved optical measurement (see Methods) of Fig. 1 (c), the plasma also expands longitudinally (along the z-axis) in vacuum, forming an expanding cone of 30° half-angle around the z-axis [3]. The magnetic field is also advected with the plasma flow away from the target surface along the z-axis [4] and one can observe from Fig. 1 (c) that the plasma expands longitudinally over more than 0.5 mm in 1.5 ns. At the outermost tip of the expansion along the z-axis, the magnetic field strength is lowered to $\sim 20 - 50$ T [4, 5].

In our double target configuration, the targets are distanced from each other by α along their normal (see Fig. 1 (a)), and when we let the two plasma plumes interact, as shown in Fig. 1 (d), the optical measurement reveals that there is a clear density pile-up in between the two plasmas, and that this pile-up follows an axis that is rotated by 45° compared the the target normal (see the yellow dashed line).

To characterize the individual magnetic field structures produced by each plasma, as well as the compression produced by their encounter in the region between the two targets, we use proton radiography [6] (see Methods). This diagnostic yields the magnetic field distribution in strength and spatial in the xy-plane.

The experimental films shown in Fig. 2 (a1-a3) display the dose modulations recorded by 6.6 MeV protons of the magnetic fields on a single T1 target (a1), on a single T2 target (a2), and when both T1 and T2 targets are present (a3). Note that in the latter case, we have chosen the separation between the targets α (here equals to 400 μm) to be such that it is smaller than the longitudinal (along the z-axis) extent of a single flux tube

* julien.fuchs@polytechnique.edu

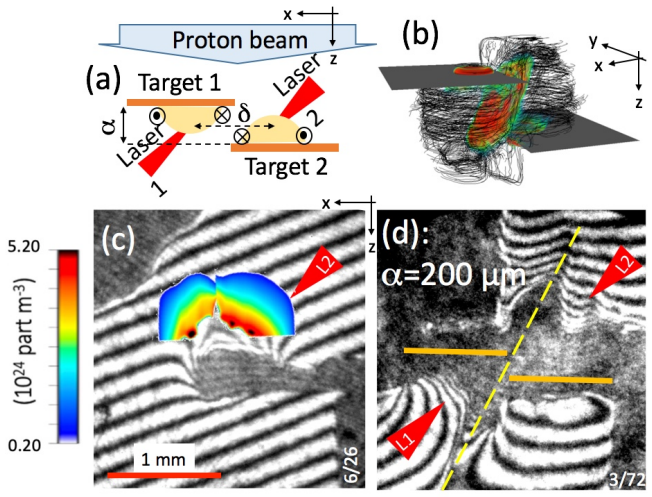

FIG. 1. (a) Schematic diagram of the experiment in the xz-plane, using two lasers (L1 and L2, separated at focus by $\delta = 500$ μm along the x-axis) and two targets (T1 and T2, separated along the x-axis by a variable distance α). Also shown are the protons (in light blue, sent along the z-axis) used for the radiography diagnostic (see Methods) and the plasma plumes with frozen-in magnetic flux tube generated by each laser ablation at the target front (in yellow). (b) 3D simulated (see Methods) depiction of the magnetic field lines in the flux tubes (in black), together with the compressed magnetic sheet in between the two plasmas (in colour), snapshot at $t\Omega_0 = 37$. (c-d) Raw optical interferometry images of (c) just one plasma expanding from T2, and (d) the two plasmas, in the xz-plane. The time at which the snapshot are taken are, respectively, (c) 1.5 and (d) 3 ns after the start of the laser irradiation of the targets. In panel (c) is shown the deconvolved volumetric density map, illustrating, as expected, the plasma expansion along the target normal, i.e. along the z-axis. In (d), the initial locations of the T1 and T2 targets are indicated by the orange lines.

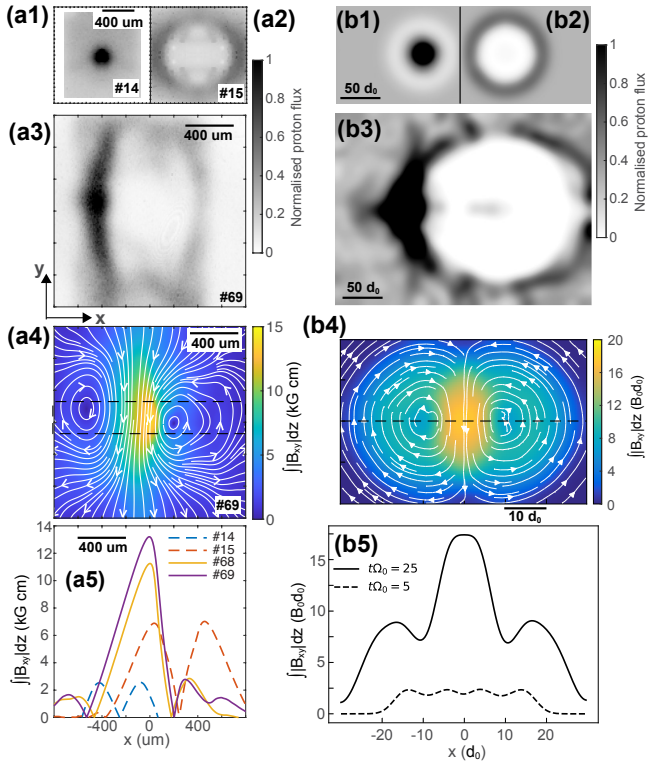

FIG. 2. (a1-a2) Experimental proton-radiography images (see Methods) probing the single magnetic flux tubes produced on (a1) target T2 or (a2) target T1. Both images are snapshots taken at at 1 ns. (a3) Same but when there are the two targets (snapshot at 2.25 ns). (a4) Path-integrated magnetic field strength analyzed via the code PROBLEM [7]. The white-arrow streamlines represent the in-plane magnetic field lines (B_x and B_y), and the colormap shows the path-integrated (along the z-axis) strength of the xy-plane magnetic field. (a5) Lineout, along the z-axis, of the path-integrated magnetic field strength (measured in the black dashed box shown in panel (a4) and averaged along the y-axis). Also shown are the lineouts corresponding to the images shown in panels (a1-a2) and for another shot (#68) where the two plasmas interact at an earlier time, i.e. 1.25 ns. The right column shows the corresponding results obtained from the hybrid simulations (see Methods). The synthetic proton dose distributions are shown for the two targets case (b1-b2) before and (b3) after their interaction. (b4) The path-integrated magnetic field strength distribution in the xy-plane of the simulation box (at $t\Omega_0 = 25$), along with (b5) the lineout taken along the black dashed line (at $y = 0$) shown in panel (b4).

for the times considered here, as inferred from the optical probing data. This allows us to make sure of the overlap between the two flux tubes. Since the direction of the magnetic fields from the two targets relative to the probing proton beam are opposite (see Fig. 1 (a)), therefore the magnetic fields affect the probing proton beam in opposite ways. When there is only a plasma expanding from the T2 target, the magnetic field structure focuses the proton beam, leading to a concentrated proton dose (see Fig. 2 (a1)), as expected [8, 9]. Conversely, [8, 9], the proton deflection pattern is reversed when there is only a plasma expanding from the T1 target, as the magnetic field structure now defocuses the proton beam, yielding a radiograph characterized by a large white ring structure surrounded by a dark ring, the probing protons having been expelled from within, and to be accumulated at the edge (see Fig. 2 (a2)). Now, when the two plasmas are simultaneously expanding from the T1 and T2 targets, the proton deflection pattern differs quite significantly from what would be the simple linear overlap of two single-plasma induced patterns. Indeed, as can be seen in Fig. 2 (a3), the resulting pattern is such that the focused proton structure has now largely expanded into an arc-shape, whereas the defocused white ring is vertically stretched with a clear disruption at the top and bottom.

Such a pattern could suggest that there is a compressed region, namely an increased strength magnetic field in the two plasmas interaction region. If we assume that the probing protons propagate through the compressed magnetic field region, we can expect that they are de-

flected more towards the focused spot. This deflection is asymmetric because compression occurs only in a small region. For the same reason, the defocused ring structure is broken, with the curvature radius of the resulting structure being larger than that produced by the single flux tube.

To test this hypothesis, Figure 2 (a4) displays the path-integrated magnetic field map reconstructed from the proton deflectometry map shown in panel (a3) using the PROBLEM algorithm [7] (see Methods). Here, we can clearly distinguish the two individual flux tubes with opposite polarity, and the magnetic field build-up in between. The two flux tubes are of similar shape and magnetic field strength, as expected, since this is what we observe for the non-interacting single flux tubes corresponding to panels (a1-a2). Figure 2 (a5) shows lineouts of the path-integrated magnetic field from the map of the interacting flux tubes (panel a4, corresponding to a probing time of 2.25 ns after the start of the laser irradiation), as well as that from another shot taken at an earlier time (1.25 ns). The same panel also shows lineouts from the individual flux tubes reconstructed from panels (a1) and (a2). Note that the data for the individual flux tubes are taken early on (1 ns), in order to show that the magnetic field is then already fully developed and present at the interaction point ($x = 0$). Despite the shot-to-shot variation, one can quantitatively discern the compression of the magnetic field in the interaction zone, compared to the field in the individual flux tubes on both sides of the flux tubes encounter (B_{foot}, in reference to the standard terminology used for magnetic field compression in shocks [10]).

To quantify the level of maximum compressed magnetic field (B_{max}), we have to consider that the effective compression in the three-dimensional structures flux tubes takes place only over a fraction (h) of the maximum possible interacting length α (see Fig. 1 (a)). Thus, one can write in the interaction zone (i.z.): $\int_{i.z.} Bdz = B_{max}h + B_{foot}(\alpha - h)$. Since we have, for the non-interacting outer region, $\int_{out} Bdz \approx B_{foot}\alpha$, it leads to: $B_{max}/B_{foot} \approx 1 + (\int_{i.z.} Bdz/\int_{out} Bdz - 1)(\alpha/h)$. We infer from Fig. 2 (a5) that $(\int_{i.z.} Bdz/\int_{out} Bdz) \sim 2-4$, while our simulations detailed below suggest that $\alpha/h \sim 2-4$, thus yielding a compression level of $B_{max}/B_{foot} \sim 3-5$. We stress that the data shown in Fig. 2 is only a subset of the overall data taken during our experiments, in all of which we have observed the same range for the maximum magnetic compression.

The limited magnetic compression observed in the experiments could seem surprising, given that much higher compression ratios, i.e. up to thousands, could be obtained when an overall distributed magnetic field is compressed, e.g. radially or by a shock [11–13]. To investigate the dynamics underlying the observed limited compression, we performed numerical simulations with the the 3D hybrid PIC code AKA [14] (see Methods). Just as in the experiments, we can simulate one single flux tube, or the interaction between two flux tubes. The

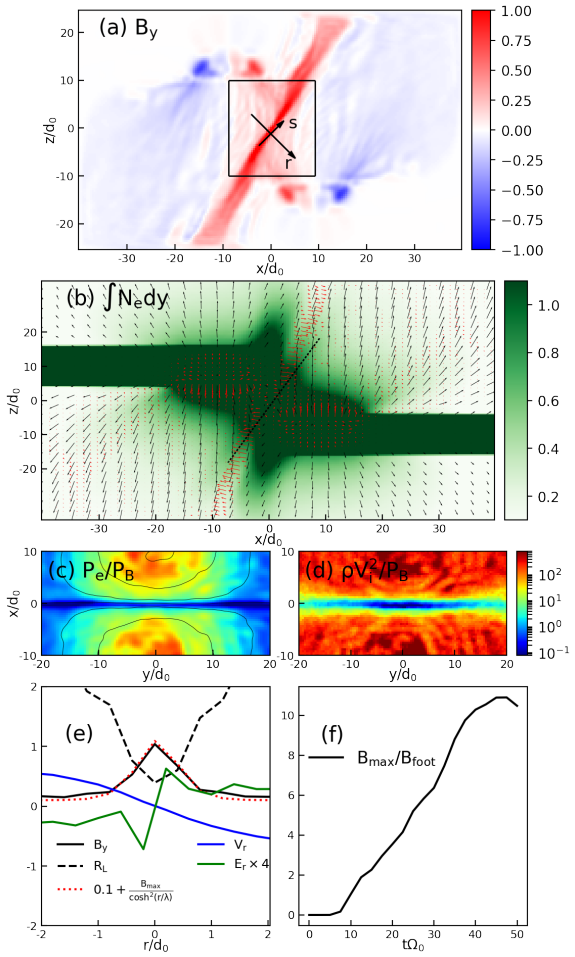

FIG. 3. Simulation results of (a) B_y (normalized to B_0, see Methods) in the two interacting plasmas with their magnetic flux tubes at $t\Omega_0 = 50$ for $\alpha = 20d_0$, (b) integrated electron density (normalized to $n_0 d_0$, see Methods) at $t\Omega_0 = 50$ for $\alpha = 10d_0$ with superposed associated electric fields (red arrows) and ion flows (black arrows); the black line line marks the integrated density in between the two plasmas, which is markedly slanted, similarly as in the experimental image of Fig. 2 (d), (c) plasma beta (i.e., ratio of the electron pressure to magnetic pressure) with superposed magnetic field lines in black, and (d) ratio of the ion flow ram pressure to the magnetic pressure at $t\Omega_0 = 50$ for $\alpha = 20d_0$. (e) Lineouts along the auxiliary axis r (see panel (a)) of the flow velocity (normalized to the Alfvén velocity V_A, in blue), electric field E_r (in units of cB_0, green), ion Larmor radius R_L (in units of d_0, dashed), accumulated magnetic field B_y (in units of B_0, black) and an approximation by the solitary solution $0.1 + B_{max}cosh^{-2}(r/\lambda)$ with λ=1.2 (red). (f) Time evolution of the magnetic compression for $\alpha = 20d_0$.

simulation program also has the capability of producing synthetic proton radiographs. These, as shown in Fig. 2 (b1-b3), are in good qualitative agreement with the features observed in the experiments. As we will now detail, the limited compression can be mostly understood in the frame of ideal MHD. Fundamentally, that limitation is

the consequence of an induced electric field ($\mathbf{V}_{flow} \times \mathbf{B}$, in which $\mathbf{V}_{flow}$ is the flow velocity and $\mathbf{B}$ is the magnetic field) that is present on both sides of the compressed magnetic sheet. This field acts to deflect the inflows coming onto that sheet, and therefore limiting further compression of the frozen-in magnetic field. It is also this deflection that induces the slanted pile-up density structure that is experimentally observed in Fig. 1 (d).

The same slanted structure is observed in the simulations, as shown in Figure 3 (a) that displays the $y-z$ map of the interacting flux tubes at the end of the simulation, i.e. at $t\Omega_0 = 50$ for $\alpha = 20d_0$ (see definition in Methods). As shown by their decreasing Larmor radius (see the dashed line in Figure 3 (e)), we observe that the ions approaching the compressed magnetic sheet become magnetized. Furthermore, as shown in Figure 3 (c,d) we observe that both the electrons and ions are magnetized near the magnetic sheet: there, the plasma beta parameter for both the electrons (i.e. the ratio of the electron pressure to the magnetic field pressure) and the ions (i.e., the ratio of the ion ram pressure ρV_{flow}^2, where ρ is the plasma density, to the magnetic pressure) stays < 1. This is further confirmed by the fact that, as shown by the full black and dashed red lines in Fig. 3 (e), the quasi-stationary compressed magnetic sheet can be very well approximated by the stationary solitary solution $\sim B_{max} cosh^{-2}(r/\lambda)$ (where λ is the width of the magnetic sheet) of the classical current sheet of the Harris equilibrium of magnetic reconnection [15].

Once the magnetic sheet width becomes approximately equal to two ion Larmor radii, the ions cannot leave the sheet. Subjected to the induced electric field $\sim \mathbf{V}_{flow} \times \mathbf{B}$, they then merely drift in the outflow direction (the $s-axis$ in Figure 3.a). This is illustrated in Figure 3.b which shows the (integrated along the $y-axis$) electron density, together with the electric fields (red arrows), and ion flow velocities (black arrows). The ion dynamics, as they approach the magnetic sheet, is illustrated in Figure. 4, which represents the ions in the phase space (r,V_r). In the single flux tube case (Figure. 4.a), i.e. when there is no magnetic sheet hindering the ions flow, we observe that the V_r velocity of the ions stay quite constant. On the contrary, in the case of the interacting flux tubes (Figure. 4.b), we observe that the ions flows V_r velocity reduces on both sides of the magnetic sheet, as the ions are effectively redirected along the sheet (see the black arrows in Figure 3 (b)) by the associated electric field. Additionally, comparing the ions distribution functions for the cases with (Figure. 4.c) and without (Figure. 4.b) the Hall term included in the modeling of the Ohm's law (see Methods), we notice in the latter case the increase of the deceleration and of the reflection of the ions inside the sheet. Although the ideal MHD framework can capture the essence of the dynamics, non-ideal effects render the magnetic field accumulation and its effects on the ion flows stronger.

To estimate the compressed magnetic field strength B_{max}, we recognize that the characteristic width of the compressed magnetic sheet is not only equal to twice the ion gyroradius ($r_{Li} = V_{flow}/\Omega_{ci}$ where Ω_{ci} is the ion cyclotron frequency), but is also equal to the ion inertial length [10, 16–18], which can also be written as $d_0 = V_A/\Omega_{ci}$, where V_A is the Alfvén velocity. Hence, at the foot of the magnetic sheet, the Alfvén velocity becomes approximately equal to the double of the plasma flow velocity, from which we deduce that $B_{max} = 2V_{flow}\sqrt{\mu_0 m_i n_i}$. Since, at the point where the velocity and magnetic field profiles cross, $V_{flow}/V_A = 0.27$ (see the blue curve in Figure 3.(e)) and $n_e/n_0 \sim 2.5$ at the same location, we obtain $B_{max}/B_0 \sim 1$. We can also measure in the simulation $B_{foot}/B_0 = 0.1$, which then yields $B_{max}/B_{foot} \sim 10$, i.e. close to what is observed in the simulation (see Fig. 3.f).

We note that the simulated value is higher than the experimentally retrieved one; this can understood with the fact that the simulation is perfectly symmetric, which allows for stronger compression. Nonetheless we can see that there is a limited compression.

We have pinpointed a mechanism that can explain the very modest compression factor observed at all scales in the Universe during the interaction of two magnetic field structures advected by matter, whether galactic or star-emitted. Magnetic fields are not only a major source of energy in many processes, such as jet formation [19]

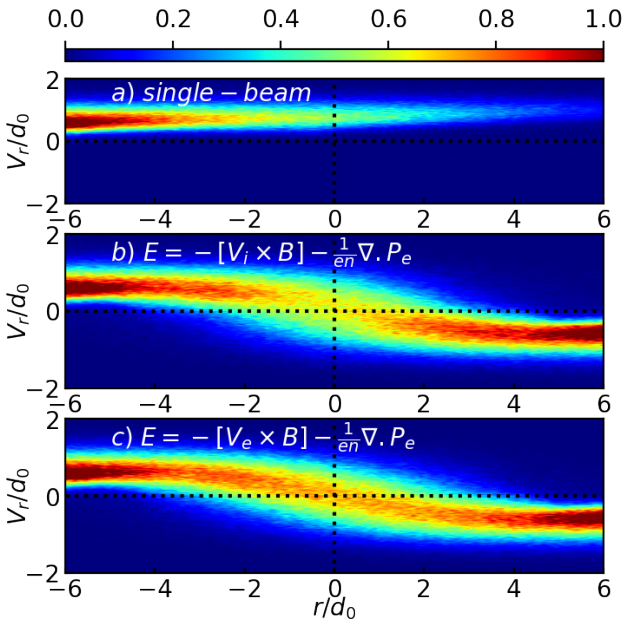

FIG. 4. Phase space (r,V_r) for the particles in the black rectangle in Fig. 3.a at $t\Omega_0 = 50$. The coordinates (r,s) correspond to the two perpendicular axes in the plane $x-z$ shown in Fig. 3 (a), i.e. the unit vector r, which is along the normal to the magnetic sheet, and s, which is along the magnetic sheet. The particles number represented by the colorbar is normalized to N_{max}. (a) for the single-beam case (a), for the two targets without Hall effect in Ohm's law (b) and for the two targets with the Hall effect included.

or cosmic-ray acceleration [20], but also affect fundamental processes like thermal conduction and radiative cooling in optically thin plasma [21], and as well modify the dynamics of astrophysical objects at every scale, ranging from the formation of stars [22, 23] and galaxies [24] to the dynamics of accretion disks [25, 26] and solar phenomena [27, 28]. We thus anticipate that our results will help to enhancing the comprehension of all these phenomena, through an understanding of the dynamics of the magnetic field regulating them. Indeed, when two plasmas carrying magnetic field interact, as e.g. in configurations as varied as galaxy-cluster [29], supernova remnant-cloud [30] or wind-exoplanet [31] configurations, the overall magnetic field will be affected, as analysed here, thereby impacting the future evolution of the system.

This laboratory approach bears promises to extend the investigation to the strong magnetic compression suggested by observations [32] in the collisionless relativistic plasmas of gamma-ray bursts, and which is thought [33, 34] to be at the source of the large and highly energetic synchrotron emissions observed to originate from them. This should now be possible using existing ultra-intense lasers [35], capable of producing highly relativistic electrons [36] and ultra-strong magnetic fields [37, 38].

ACKNOWLEDGMENTS

We acknowledge useful discussions with S. Orlando (INAF), T. Vinci (LULI) and A. Strugarek (CEA). We thank the LULI teams for their expert technical support. This work was supported by the European Research Council (ERC) under the European Union's Horizon 2020 research and innovation program (Grant Agreement No. 787539). T.W. acknowledges the financial support of the IdEx University of Bordeaux / Grand Research Program "GPR LIGHT".

[1] L. Biermann and A. Schlüter, Cosmic radiation and cosmic magnetic fields. ii. origin of cosmic magnetic fields, Physical Review **82**, 863 (1951).
[2] K. M. Schoeffler, N. F. Loureiro, R. Fonseca, and L. Silva, The generation of magnetic fields by the biermann battery and the interplay with the weibel instability, Physics of Plasmas **23** (2016).
[3] D. Higginson, G. Revet, B. Khiar, J. Béard, M. Blecher, M. Borghesi, K. Burdonov, S. Chen, E. Filippov, D. Khaghani, K. Naughton, H. Pépin, S. Pikuz, O. Portugall, C. Riconda, R. Riquier, S. Ryazantsev, I. Skobelev, A. Soloviev, M. Starodubtsev, T. Vinci, O. Willi, A. Ciardi, and J. Fuchs, Detailed characterization of laser-produced astrophysically-relevant jets formed via a poloidal magnetic nozzle, High Energy Density Physics **23**, 48 (2017).
[4] P. Campbell, C. Walsh, B. Russell, J. Chittenden, A. Crilly, G. Fiksel, P. Nilson, A. Thomas, K. Krushelnick, and L. Willingale, Magnetic signatures of radiation-driven double ablation fronts, Physical Review Letters **125**, 10.1103/physrevlett.125.145001 (2020).
[5] S. Bolaños, A. Sladkov, R. Smets, S. N. Chen, A. Grisollet, E. Filippov, J.-L. Henares, V. Nastasa, S. Pikuz, R. Riquier, et al., Laboratory evidence of magnetic reconnection hampered in obliquely interacting flux tubes, Nature Communications **13**, 6426 (2022).
[6] D. B. Schaeffer, A. F. Bott, M. Borghesi, K. A. Flippo, W. Fox, J. Fuchs, C. Li, F. H. Séguin, H.-S. Park, P. Tzeferacos, and L. Willingale, Proton imaging of high-energy-density laboratory plasmas, Reviews of Modern Physics **95**, 10.1103/revmodphys.95.045007 (2023).
[7] A. Bott, C. Graziani, P. Tzeferacos, T. White, D. Lamb, G. Gregori, and A. Schekochihin, Proton imaging of stochastic magnetic fields, Journal of Plasma Physics **83**, 905830614 (2017).
[8] C. Cecchetti, M. Borghesi, J. Fuchs, G. Schurtz, S. Kar, A. Macchi, L. Romagnani, P. Wilson, P. Antici, R. Jung, et al., Magnetic field measurements in laser-produced plasmas via proton deflectometry, Physics of Plasmas **16**, 043102 (2009).
[9] R. D. Petrasso, C. K. Li, F. H. Seguin, J. R. Rygg, J. A. Frenje, R. Betti, J. P. Knauer, D. D. Meyerhofer, P. A. Amendt, D. H. Froula, O. L. Landen, P. K. Patel, J. S. Ross, and R. P. J. Town, Lorentz mapping of magnetic fields in hot dense plasmas, Physical Review Letters **103**, 10.1103/physrevlett.103.085001 (2009).
[10] A. Balogh and R. A. Treumann, Physics of collisionless shocks: space plasma shock waves (Springer Science & Business Media, 2013).
[11] O. Gotchev, P. Chang, J. Knauer, D. Meyerhofer, O. Polomarov, J. Frenje, C. Li, M.-E. Manuel, R. Petrasso, J. Rygg, et al., Laser-driven magnetic-flux compression in high-energy-density plasmas, Physical review letters **103**, 215004 (2009).
[12] D. Nakamura, A. Ikeda, H. Sawabe, Y. Matsuda, and S. Takeyama, Record indoor magnetic field of 1200 t generated by electromagnetic flux-compression, Review of Scientific Instruments **89**, 095106 (2018).
[13] J. Giacalone and J. R. Jokipii, Magnetic field amplification by shocks in turbulent fluids, The Astrophysical Journal **663**, L41 (2007).
[14] A. Sladkov, Aka code, https://zenodo.org/records/10435108 (2023).
[15] E. G. Harris, On a plasma sheath separating regions of oppositely directed magnetic field, Il Nuovo Cimento (1955-1965) **23**, 115 (1962).
[16] R. Sagdeev, Cooperative phenomena and shock waves in collisionless plasmas, Reviews of plasma physics **4**, 23 (1966).
[17] D. Biskamp and H. Welter, Numerical studies of magnetosonic collisionless shock waves, Nuclear Fusion **12**, 663 (1972).
[18] D. Schaeffer, W. Fox, D. Haberberger, G. Fiksel, A. Bhattacharjee, D. Barnak, S. Hu, and K. Germaschewski, Generation and evolution of high-mach-number laser-driven magnetized collisionless shocks in the laboratory, Physical review letters **119**, 025001 (2017).

[19] B. Albertazzi, A. Ciardi, M. Nakatsutsumi, T. Vinci, J. Béard, R. Bonito, J. Billette, M. Borghesi, Z. Burkley, S. Chen, et al., Laboratory formation of a scaled protostellar jet by coaligned poloidal magnetic field, Science **346**, 325 (2014).

[20] A. Bell, K. Schure, B. Reville, and G. Giacinti, Cosmic-ray acceleration and escape from supernova remnants, Monthly Notices of the Royal Astronomical Society **431**, 415 (2013).

[21] S. Orlando, F. Bocchino, F. Reale, G. Peres, and P. Pagano, The importance of magnetic-field-oriented thermal conduction in the interaction of snr shocks with interstellar clouds, The Astrophysical Journal **678**, 274–286 (2008).

[22] M. R. Krumholz and C. Federrath, The Role of Magnetic Fields in Setting the Star Formation Rate and the Initial Mass Function, Frontiers in Astronomy and Space Sciences **6**, 7 (2019), arXiv:1902.02557 [astro-ph.GA].

[23] A. Bracco, D. Bresnahan, P. Palmeirim, D. Arzoumanian, P. André, D. Ward-Thompson, and A. Marchal, Compressed magnetized shells of atomic gas and the formation of the Corona Australis molecular cloud, Astronomy & Astrophysics **644**, A5 (2020), arXiv:2010.10110 [astro-ph.GA].

[24] A. Müller, B. M. Poggianti, C. Pfrommer, B. Adebahr, P. Serra, A. Ignesti, M. Sparre, M. Gitti, R.-J. Dettmar, B. Vulcani, and A. Moretti, Highly ordered magnetic fields in the tail of the jellyfish galaxy JO206, Nature Astronomy **5**, 159 (2020).

[25] D. Seifried, R. Banerjee, R. S. Klessen, D. Duffin, and R. E. Pudritz, Magnetic fields during the early stages of massive star formation - I. Accretion and disc evolution, Monthly Notices of the Royal Astronomical Society **417**, 1054 (2011), arXiv:1106.4485 [astro-ph.SR].

[26] J. Zamponi, M. J. Maureira, B. Zhao, H. B. Liu, J. D. Ilee, D. Forgan, and P. Caselli, The young protostellar disc in IRAS 16293-2422 B is hot and shows signatures of gravitational instability, Monthly Notices of the Royal Astronomical Society **508**, 2583 (2021), arXiv:2109.06497 [astro-ph.SR].

[27] M. J. Owens and R. J. Forsyth, The Heliospheric Magnetic Field, Living Reviews in Solar Physics **10**, 5 (2013).

[28] V. B. Belakhovsky, V. A. Pilipenko, Y. A. Sakharov, D. L. Lorentzen, and S. N. Samsonov, Geomagnetic and ionospheric response to the interplanetary shock on January 24, 2012, Earth, Planets and Space **69**, 105 (2017).

[29] B. Vollmer, M. Soida, R. Beck, M. Urbanik, K. T. Chyży, K. Otmianowska-Mazur, J. D. P. Kenney, and J. H. van Gorkom, The characteristic polarized radio continuum distribution of cluster spiral galaxies, Astronomy & Astrophysics **464**, L37–L40 (2007).

[30] S. Orlando, M. Miceli, O. Petruk, M. Ono, S. Nagataki, M. A. Aloy, P. Mimica, S. H. Lee, F. Bocchino, G. Peres, and M. Guarrasi, 3D MHD modeling of the expanding remnant of SN 1987A. Role of magnetic field and non-thermal radio emission, Astronomy & Astrophysics **622**, A73 (2019), arXiv:1812.00021 [astro-ph.HE].

[31] G. B. Trammell, P. Arras, and Z.-Y. Li, Hot jupiter magnetospheres, The Astrophysical Journal **728**, 152 (2011).

[32] R. Santana, R. Barniol Duran, and P. Kumar, Magnetic fields in relativistic collisionless shocks, The Astrophysical Journal **785**, 29 (2014).

[33] G. R. da Silva, D. Falceta-Gonçalves, G. Kowal, and E. M. de Gouveia Dal Pino, Ambient magnetic field amplification in shock fronts of relativistic jets: an application to grb afterglows, Monthly Notices of the Royal Astronomical Society **446**, 104–119 (2014).

[34] A. Pe'er, Plasmas in gamma-ray bursts: Particle acceleration, magnetic fields, radiative processes and environments, Galaxies **7**, 33 (2019).

[35] C. N. Danson, C. Haefner, J. Bromage, T. Butcher, J.-C. F. Chanteloup, E. A. Chowdhury, A. Galvanauskas, L. A. Gizzi, J. Hein, D. I. Hillier, N. W. Hopps, Y. Kato, E. A. Khazanov, R. Kodama, G. Korn, R. Li, Y. Li, J. Limpert, J. Ma, C. H. Nam, D. Neely, D. Papadopoulos, R. R. Penman, L. Qian, J. J. Rocca, A. A. Shaykin, C. W. Siders, C. Spindloe, S. Szatmári, R. M. G. M. Trines, J. Zhu, P. Zhu, and J. D. Zuegel, Petawatt and exawatt class lasers worldwide, High Power Laser Science and Engineering **7**, 10.1017/hpl.2019.36 (2019).

[36] A. Gonsalves, K. Nakamura, J. Daniels, C. Benedetti, C. Pieronek, T. de Raadt, S. Steinke, J. Bin, S. Bulanov, J. van Tilborg, C. Geddes, C. Schroeder, C. Tóth, E. Esarey, K. Swanson, L. Fan-Chiang, G. Bagdasarov, N. Bobrova, V. Gasilov, G. Korn, P. Sasorov, and W. Leemans, Petawatt laser guiding and electron beam acceleration to 8 gev in a laser-heated capillary discharge waveguide, Physical Review Letters **122**, 10.1103/physrevlett.122.084801 (2019).

[37] A. Flacco, J. Vieira, A. Lifschitz, F. Sylla, S. Kahaly, M. Veltcheva, L. O. Silva, and V. Malka, Persistence of magnetic field driven by relativistic electrons in a plasma, Nature Physics **11**, 409–413 (2015).

[38] M. Lamač, U. Chaulagain, J. Nejdl, and S. V. Bulanov, Generation of intense magnetic wakes by relativistic laser pulses in plasma, Scientific Reports **13**, 10.1038/s41598-023-28753-3 (2023).

[39] M. Rosenberg, C. Li, W. Fox, I. Igumenshchev, F. Séguin, R. Town, J. Frenje, C. Stoeckl, V. Glebov, and R. Petrasso, First experiments probing the collision of parallel magnetic fields using laser-produced plasmas, Physics of Plasmas **22**, 042703 (2015).

[40] A. Y. Faenov, S. A. Pikuz, A. I. Erko, B. A. Bryunetkin, V. M. Dyakin, G. V. Ivanenkov, A. R. Mingaleev, T. A. Pikuz, V. M. Romanova, and T. A. Shelkovenko, High-performance x-ray spectroscopic devices for plasma microsources investigations, Physica Scripta **50**, 333 (1994).

[41] L. Lancia, B. Albertazzi, C. Boniface, A. Grisollet, R. Riquier, F. Chaland, K.-C. Le Thanh, P. Mellor, P. Antici, S. Buffechoux, et al., Topology of megagauss magnetic fields and of heat-carrying electrons produced in a high-power laser-solid interaction, Physical review letters **113**, 235001 (2014).

[42] L. Gao, P. Nilson, I. Igumenshchev, M. Haines, D. Froula, R. Betti, and D. Meyerhofer, Precision mapping of laser-driven magnetic fields and their evolution in high-energy-density plasmas, Physical review letters **114**, 215003 (2015).

[43] M. M. Sulman, J. Williams, and R. D. Russell, An efficient approach for the numerical solution of the monge–ampère equation, Applied Numerical Mathematics **61**, 298 (2011).

[44] C. Palmer, P. Campbell, Y. Ma, L. Antonelli, A. Bott, G. Gregori, J. Halliday, Y. Katzir, P. Kordell, K. Krushelnick, et al., Field reconstruction from proton radiography of intense laser driven magnetic reconnection, Physics of Plasmas **26**, 083109 (2019).

[45] J. J. MacFarlane, I. E. Golovkin, P. R. Woodruff, D. R.

Welch, B. V. Oliver, T. A. Melhorn, R. B. Campbell, T. A. Mehlhorn, and R. B. Campbell, Simulation of the ionization dynamics of aluminum irradiated by intense short-pulse lasers, Proceedings of Inertial Fusion and Science Applications (American Nuclear Society, La Grange Park, IL) , 1 (2003).

[46] R. Weber, R. Giedl-Wagner, D. J. Förster, A. Pauli, T. Graf, and J. E. Balmer, Expected X-ray dose rates resulting from industrial ultrafast laser applications, Applied Physics A: Materials Science and Processing **125**, 10.1007/s00339-019-2885-1 (2019).

[47] T. Takizuka and H. Abe, A binary collision model for plasma simulation with a particle code, Journal of computational physics **25**, 205 (1977).

METHODS

General experimental setup: The experiments were performed at two different high-intensity laser facilities, namely LULI2000 (France) and VULCAN (Rutherford Appleton Laboratory, U.K.), which both have similar laser parameters, in order to field complementary diagnostics on the interested plasma interaction. We note that in a previous experiment [39], using a similar configuration, they were not able to measure any magnetic field compression, likely due to the short duration over which the magnetic fields were generated and a too large distance between the magnetic fields, thereby weakening magnetic compression. In our experiment, two 5 μm thick copper targets (T1 and T2) were irradiated by two laser beams (L1 and L2, having ~ 35 GW power over up to 5 ns and focused over azimuthally averaged radii of ~ 25 μm circular focal spots, yielding on-target intensity of $\sim 10^{15}$ W/cm^2). The laser irradiation on the two targets generated two hot, dense plasmas that expand radially toward each other. A time-integrated x-ray spectrometer with spatial resolution (FSSR) [40], which records L-shell lines from the copper plasma (see below), allowed us to determine the peak electron temperature in the laser-irradiated region to be ~ 300 eV with an average ionization level of 19. Regarding the separation between the two targets, we note that, as previously recorded [41] using similar laser conditions, the radial magnetic field expansion is ~ 300 μm/ns. Therefore, we chose the separation between the two laser impacts to be, along the x-axis, $\delta = 500$ μm (see Fig. 1 (a)), such that there is overlap between the two magnetic flux tubes within the first ns of the magnetic field generation. In each plume, the density and temperature gradients generate the so-called Biermann-Battery magnetic fields [1, 2]. Detailed characterization [5, 41, 42] of the magnetic fields were performed in similar experimental conditions and had shown that the overall topology of each magnetic field is analog to a flux tube connected to itself (see Fig. 1 (a-b)). Around the laser energy deposition zone, the magnetic field is further compressed toward the target by the Nernst effect [41, 42], reaching strength ~ 100 T for the entire laser pulse duration.

Optical interferometry: The plasma electron density is recorded by optically probing the plasma (using a milliJoule energy, 10 ns duration, 527 nm wavelength auxiliary laser pulse), coupled to Kentech gated optical imagers, in order to have a snapshot of the plasma over duration of 100 ps, and using a standard Mach-Zehnder interferometry setup. It allows to measure electron plasma densities in the range of 10^{17} cm^{-3} to 10^{19} cm^{-3}. Note that in the images the dark zone located close to the targets is due to refraction of the optical probe. Therefore this diagnostic method does not provide information about the dense plasma close to the surface of the target.

Proton radiography: A short pulse, CPA laser capable of delivering ~ 50J, $\sim 10^{19}$ W/cm^2 was incident on 25μm aluminium or Mylar targets to create a broadband,

divergent proton beam through a sheath-acceleration (TNSA) mechanism [6]. This proton beam was the probe that was used to sample [6] the magnetic fields generated in the system. A radiochromic film (RCF) stack consisting of layers of Gafchromic HDV2 and EBT3 was used as the radiography detector. The distance between the proton source and midpoint between T1 and T2 was 9.66 mm. Additionally, the distance between the copper targets and the RCF stack was 90 mm, giving a geometric magnification of $\sim$ 10.3. Separate RCFs of the same type were calibrated by physicists of the Central Laser Facility (England) using the University of Birmingham cyclotron. Through scanning the calibrated and experimental RCFs on the same scanner (EPSON Precision 2450), a model relating the optical density and dose was determined allowing all experimental RCFs to be converted into proton-deposited dose.

Magnetic field retrieval using PROBLEM: The proton radiography analysis code PROBLEM (PROton-imaged B-field nonLinear Extraction Module) was used to extract the path-integrated magnetic field from the experimental RCFs [7]. Fields are retrieved through solving the logarithmic parabolic Monge-Ampère equation for the steady state solution of the deflection field potential. This is achieved through using an adaptive mesh and a standard centred second order finite difference scheme for the spatial discretization and a forward Euler scheme for the temporal discretization [43]. The perpendicular deflection field and therefore the path-integrated magnetic field can then be calculated using the solution to the Monge-Ampère equation [7]. PROBLEM can only provide a unique solution provided there are no caustics. The contrast parameter, μ, was calculated using the equation found in [44] and was determined at a maximum (in the amplified region due to compression) to be $\mu \sim 0.3$. Radiography was therefore conducted in either linear or non-linear injective regimes.

X-ray spectroscopy: A focusing spectrometer with spatial resolution (FSSR) was used for x-ray measurements. The FSSR was equipped with a spherically bent mica crystal with a lattice spacing $2d = 19.9149$ Å and a curvature radius of $R = 150$ mm. The crystal was aligned to operate at $m = 2$ order of reflection to record the L-shell emission spectra of multicharged copper ions in the range of 8.8—9.6 Å (1290–1410 eV corresponding energy range). Spatial resolution $\delta x = 120$ μm along the compression axis was achieved. The spectral resolution was higher than Å/dÅ=1000. The spectra were recorded on a fluorescence detector Fujifilm Image Plate (IP) of TR type which was situated in a cassette holder shielded from the optical radiation. The aperture of the cassette was covered by a PET filter (2 μm thickness) coated by a thin Al (160 nm) layer to avoid the optical emission irradiating the IP. Additionally, the face of the crystal was covered by a similar filter to protect the crystal from laser-matter interaction debris and to subtract the contribution of other reflection orders to the x-ray spectra. For the measurements of the plasma parameters, we used 4d-2p and 4s-2p transitions in Ne-like ions as well as Na-like satellites which are sensitive to variations of the electron temperature and density. This emission was simulated in a steady-state approach by the PrismSPECT code [45]. A shot with two targets and large separation α (i.e. when the interaction between the two plasmas is negligible) was used to retrieve the information about the initial conditions for each plasma. In this case, we have the lowest contribution of the colder plasma zones at later stages of the evolution to the time-integrated spectrum, since this emission is blocked by the neighbour target. The Bremsstrahlung temperature was measured by fitting the spectral continuum with a theoretical profile based on the formula [46]: $dN/dE \sim A/\sqrt{T} \cdot exp(-E/kT)$.

Modeling by the code AKA: The simulation model treats the ion kinetic dynamics following the PIC formalism and describes the electrons by a 10-moment fluid (having a density which is equal to the total ion density by quasi-neutrality, a bulk velocity, and a six-component electron pressure tensor). The magnetic field and the density are normalized to B_0 and n_0, respectively. The times are normalized to the inverse of ion gyrofrequency, $\Omega_0^{-1} \equiv m_i/(Z_i e B_0)$, in which Z_i is the ionization state, e is the elementary charge, and m_i is the ion mass. The lengths are normalized to the ion inertial length $d_0 \equiv c/\omega_{pi}$, in which c is the speed of light, $\omega_{pi} = (n_0 Z_i^2 e^2/m_i/\varepsilon_0)^{1/2}$ is the ion plasma frequency, and ε_0 is the permittivity of free space. The velocities are normalized to the Alfvén velocity $V_A \equiv B_0/(\mu_0 n_0 m_i)^{1/2}$, in which μ_0 is the permeability of free space. Mass and charge are normalized to the ion ones. The normalization of the other quantities follows from these ones.

We observe that, with the plasma parameters used in the experiment, since the dimensionless Reynolds (Re), magnetic Reynolds (ReM), and Peclet (Pe) numbers are much larger than unity, the plasma flows are well approximated by the ideal MHD framework. Thus, the advective transport of momentum, magnetic field, and thermal energy dominates are dominant over diffusive transport. To mimic the ablation process, we use a heat operator pumping electron pressure in the near surface region of the targets, and a particle creation operator that sustains the constant solid target density which is equal to n_0. The ions have, as in the experiment, charge number 19 and mass number 64. These two operators create and sustain an axial electron density gradient and a radial electron temperature gradient. As a result, toroidal Biermann-battery magnetic fields are continuously produced and transported to the interaction region, where the ion flows are pressing the parallel fields against each other. The magnitude of the heat operator is adjusted to obtain the desired temperature for both ions and electrons ($T_{spot}^{e,i} = 1T_0$, which is $\sim$300 eV for the reference magnetic field B_0= 400 T and density n_0= 1.3×10^{21} cm^{-3}, as inferred from the experimental measurements). The FWHM of the heated area is $8d_0$ ($\sim 90\mu m$). The distance between the focal spot centers is set to $18d_0$ ($\sim 200\mu m$) and the α parameter is varied. The ion-ion

collisions are taken into account with the binary collision model of Ref. [47]. Figure 5 shows the difference that can be observed in the simulations in the magnetic field transport for the cases without (a) and with (b) ion-ion collisions. We see that the collisions help to stabilize the magnetic sheet and allow for additional magnetic field advection along the sheet.

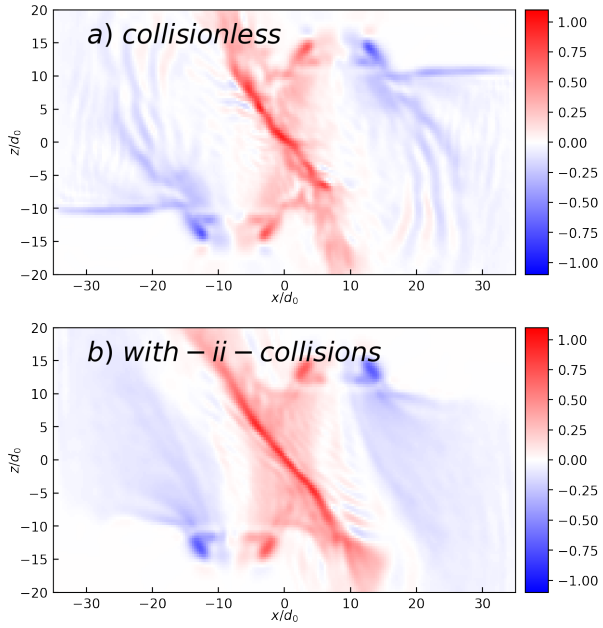

FIG. 5. B_y component of the magnetic field at $t\Omega_0 = 50$ for the modeling (a) without ion-ion collisions and (b) with moderate ion-ion collision rate.

A. COMPETING INTERESTS

The authors declare no competing interests.

B. CONTRIBUTIONS

J.F., A.Sl., M.S. and A.So. conceived the project. J.F., C.F., A.McI., S.N.C., H.A., P.M., T.W. and R.L. performed the experiments. J.F., W.Y., C.F., A.F.A.B., S.N.C., S.P., T.W. and E.D.F. analysed the data, with discussions with P.A., E.d'H., A.C. and M.B. The hybrid simulations were performed by A.Sl. The paper was mainly written by J.F., S.N.C., A.Sl., C.F., and W.Y. All authors commented and revised the manuscript.